Title

Digital Programming of Liquid Crystal Elastomers to Achieve High-Fidelity Surface Morphing

Authors

Zhai, Yichen
Tolley, Michael T
Ng, Tse Nga

Publication Date

2022-06-01

DOI

10.1016/j.apmt.2022.101501

Peer reviewed

Applied Materials Today 27 (2022) 101501

Contents lists available at ScienceDirect

Applied Materials Today

journal homepage: www.elsevier.com/locate/apmt

Digital Programming of Liquid Crystal Elastomers to Achieve High-Fidelity Surface Morphing

Yichen Zhai [a], Michael T. Tolley [b], Tse Nga Ng [a,*]

[a] Department of Electrical and Computer Engineering, University of California San Diego, La Jolla, CA 92093, USA
[b] Department of Mechanical and Aerospace Engineering, University of California San Diego, La Jolla, CA 92093, USA

A B S T R A C T

Morphable surfaces have the potential to enable new kinds of adaptive systems, but existing fabrication methods have limited ability to achieve high resolution morphing into arbitrarily specified shapes. This work presents a platform and algorithms for toolpath generation to enable freeform structures capable of high-resolution surface morphing. The morphing surfaces were composed of liquid crystal elastomer (LCE), with nematic domains aligned using a scratch post capable of applying adjustable pressure and shear velocity, offering the ability to locally tune actuation strains and thus bending curvature radii from 1.8 mm to 14.4 mm. Patterning toolpaths for multi-layer structures were generated using two alternative algorithms, the results of which were compared using example structures capable of morphing from flat sheets into domes and models of a human faces. This process resulted in morphed human face shapes with structural similarities of up to 84.5% when compared to the original model, demonstrating the high fidelity and reconfigurability of this approach for fabricating complex morphable LCE structures.

1. Introduction

Shape morphing structures have the potential to provide new approaches for the design of adaptive optics and electronics [1–4], soft robotic systems and synthetic camouflage [5–7], and human-computer interfaces [8–11]. Liquid crystal elastomers (LCE) are a type of soft material capable of topological transformations via contracting, bending, twisting, and periodical deformations upon photonic or thermal actuation [12–26] changing from a flat state into a three-dimensional (3D) shape and vice versa [27–30]. For example, the complex contours of a model of a human face have been reconstructed in a continuous LCE film [31] and in enveloping surfaces of open meshes using kirigami and origami designs [3,32–34]. However, better fidelity of the actuated LCE surface to the original design is desired, but the current design algorithms and fabrication procedures limit the pattern resolution and actuation range of the resulting morphable LCE surfaces.

To enable thermal actuation and shape shifting, the mesogens of the LCE must be aligned to form monodomains that will change their orientations upon heating. Furthermore, the strength of the alignment must be controlled to tune the stress—and consequently the strain—within the structure. This alignment has been previously achieved using molds or guides to direct the mesogen orientation based on photo-alignment [12–15] or processes directed by a catalyst [35–37], but these techniques are restricted to the patterning of thin layers and cannot adjust strain magnitudes within thick or multilayered structures. Alternatively, previous work has used digital extrusion printing to apply shear stress to align the mesogens of LCE by adjusting the velocity of the nozzle as well as the height of the nozzle with respect to the substrate [20,38,39]. Since this method couples the alignment process with the material dispensing step, the extrusion rate must be dynamically tuned with high precision, which is challenging with viscous materials like LCE. The practical result is that the patterned strain field has a limited spatial resolution.

In this report, we present a novel approach to the programmable alignment of the mesogens of layers of LCE within multilayer structures to achieve morphable surfaces with high spatial resolution. We have developed a patterning platform that decouples the material deposition and alignment processes, affording digital control using a scratch control post that applies variable pressure and shear velocity to locally tune mesogen domains within a layer of LCE. As this alignment process enables precise adjustment of strain gradients within LCE structures, we have also developed an algorithm to compile target morphing geometries into toolpaths for the patterning platform. Prior work on morphable surfaces have calculated the contraction areas in different regions required to induce out-of-plane deformations leading to three-dimensional (3D) topography [14,17,31]. By contrast, here we show that the criterion of surface curvature provides complex features with greater accuracy than mapping contraction areas. We compared two methods of curvature calculations to optimize toolpath algorithms, and we fabricated examples of printed dome and human face models to demonstrate the reconfigurability and resolution of this platform for

* Corresponding author.
E-mail address: tnn046@ucsd.edu (T.N. Ng).

https://doi.org/10.1016/j.apmt.2022.101501
Received 4 March 2022; Received in revised form 19 April 2022; Accepted 27 April 2022
Available online 5 May 2022

freeform patterning of morphable LCE structures.

2. Results

2.1. Controlling actuation curvatures of LCE

Fig. 1 show the setup for local alignment of LCE domains using a scratch post mounted on a three-axis stage. The scratch post was a metal cylinder placed under a water chamber, and a programmable syringe pump would move water in or out of the chamber to adjust the load on the post, which in turn changed the pressure applied on the LCE workpiece. The experiment procedure in this report is shown in Fig. 1**(a)**. First, individual layers of 0.2 mm thick LCE were deposited by a pneumatic extrusion printer (Raise 3D N2, with modification as specified in Ref [8]. The extrusion printing here is used for materials deposition only, not for mesogen alignment. To speed up the deposition in large scale, blade coating can also be used as alternative approach. In the second step, any alignment from the extrusion process was erased by heating the layer to ~120°C with a hot air gun. This step initialized each layer to a polydomain state. Then in the third step, the scratch post was put in contact with the LCE surface, and as the post was dragged along the surface of the uncured LCE, the horizontal shear force directed LCE mesogens to reorient from polydomains to the monodomain state. A video of the alignment process is shown in Supplemental Movie SM1. The mesogens maintained their patterned alignment for a couple of hours, a sufficiently long time for the entire surface layer to be patterned and subsequently crosslinked by a UV light to permanently set the alignment in the final step. This process was repeated for multi-layer structures, with the option to incorporate different alignment patterns for each layer.

The above approach enables the freeform alignment of LCE in patterns with arbitrary directions and magnitudes, including areas with no alignment (poly-domains) which is not possible with prior direct extrusion techniques that constrain the materials to the extrusion direction. An example of a two-layer LCE structure is shown in Fig. 1**(b)**, in which the alignment patterns on different layers can be completely different, and the pattern on each layer can be in freeform decoupled from the deposition direction.

The schematics in Fig. 2**(a)** illustrate the thermal actuation of LCE samples with the bottom two layers in weak or strong alignment, covered by two layers of polydomain films. Upon heating, the aligned layers contract while the dimensions of polydomain layers remain unchanged. As a result, the actuated structure bends into an arc or curls to a smaller radius (higher curvature) with stronger mesogen alignment. This bending mode is enabled by the multilayer design and extends the actuation of LCE beyond in-plane deformations. The photographs in Fig. 2**(b)** display the bending radii of three actuated samples sheared at the same velocity but under different loads. The actuation curvature increased as the alignment process was carried out under larger loads.

The extent of mesogen alignment and the corresponding actuation strain were adjusted by varying the shear velocity and pressure applied by the scratch post. Fig. 2**(c)** shows the bending radius of actuated samples as a function of post load and shear velocity during the alignment process. The bending radii were tunable to encompass a wide range from 1.8 mm to 14.4 mm. When the load on the scratch post was increased to higher than 6.5 g, the bending radius reached saturation. When the shear velocity was varied between 0.5 mm/s to 2 mm/s at a fixed load, there was a positive monotonic correlation, i.e., higher velocity led to an increasing radius of curvature. As the scratch post moved faster, it induced weaker mesogen alignment; and if the post velocity exceeded 2 mm/s, the post intermittently lost contact with the LCE surface, resulting in poor alignment as manifested in the irregular trend for velocity >2 mm/s as observed in the Fig. 2(c) inset. This trend is different from prior shear alignment methods [20,40], in which higher printing velocity resulted in stronger alignment. In this work, when the shear post traveled at a higher velocity, the depth of LCE that can be sheared was reduced. The uncured LCE at the bottom was not subjected to shearing force. In contrast, the prior methods aligned LCE by the relative movement between the nozzle and the substrate. With this mechanism, a higher velocity led to a higher shear rate enabling stronger alignment.

To ensure well-controlled alignment, we set the control parameters within the shaded regions in Fig. 2(c). For a target actuation curvature within the control boundaries, our tooling algorithm would select the corresponding shear velocity and load based on the calibration in Fig. 2 (c). In our calibration and experiments, we fixed the individual layer

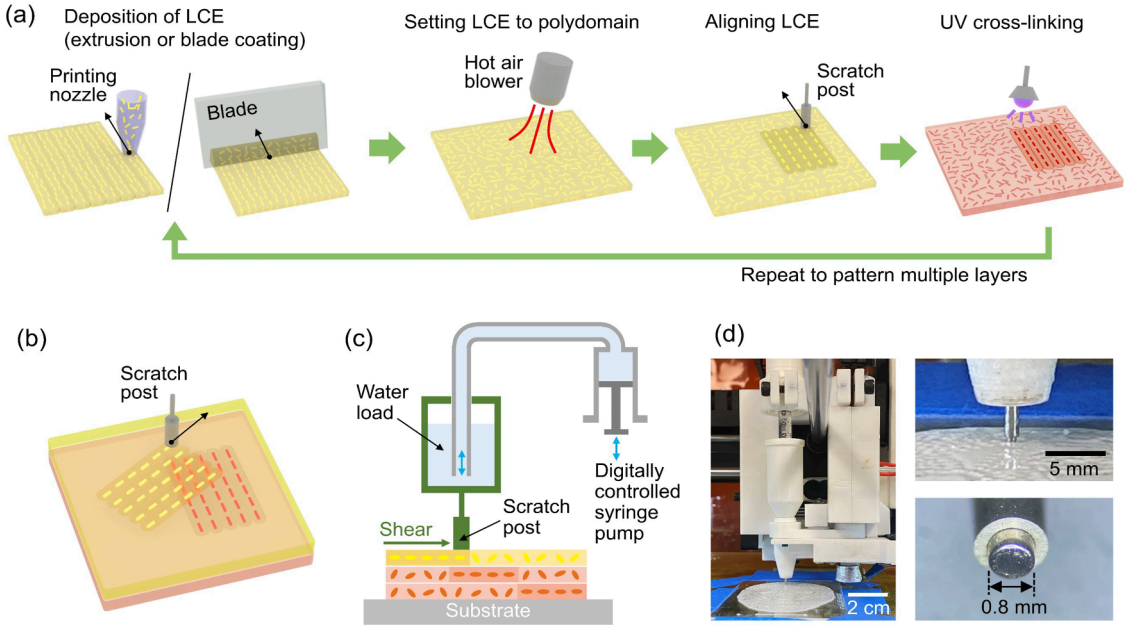

Fig. 1. (a) An iterative process to deposit and align LCE in multiple layers. (b) Illustration of freeform alignment patterns on different layers. (c) A schematic of the LCE alignment platform. In parts (a)~(c), yellow regions represent uncured LCE, and red regions represent cured LCE. (d) Photograph of the scratch post connected to a water chamber that varies the scratch load (left). Detailed side view (top right) and bottom view (bottom right) photographs of the scratch post.

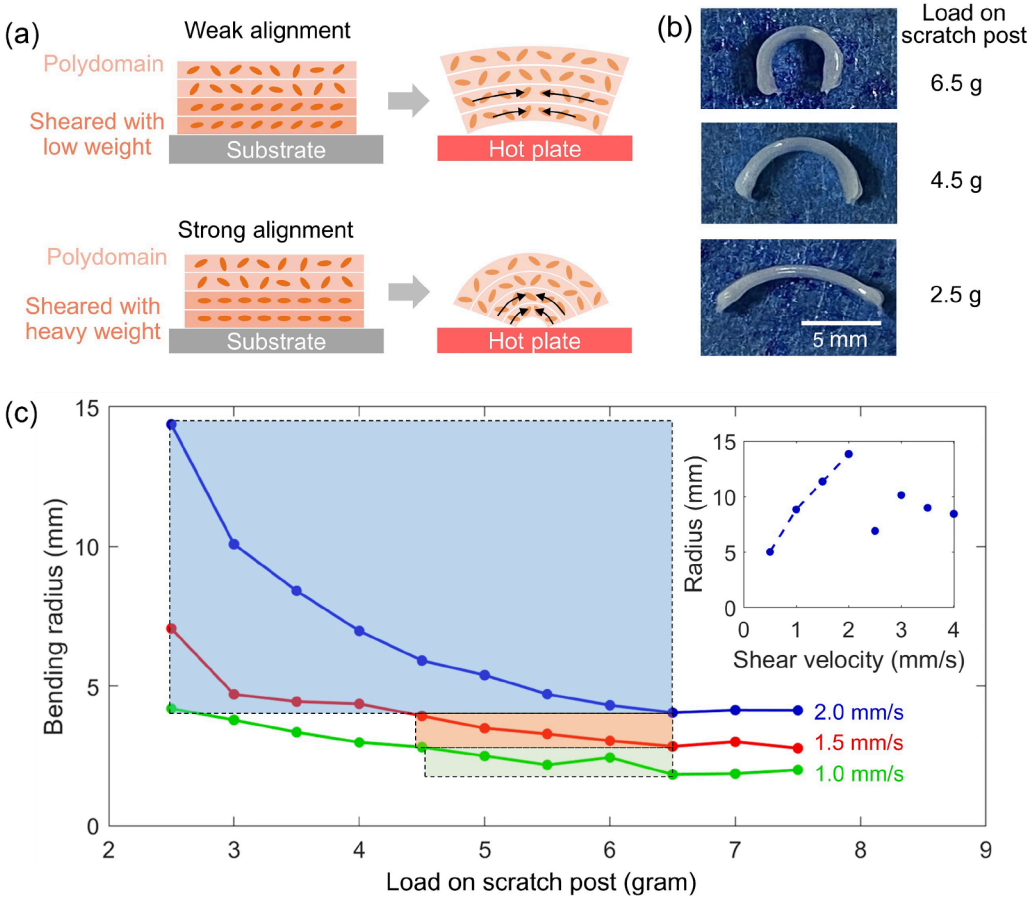

Fig. 2. (a) Illustrations of LCE domains processed under different scratch loads to control bending curvatures upon thermal actuation. (b) Photographs of thermally actuated LCE samples scratched under various loads at a post velocity of 1.5 mm/s. The samples were heated to a temperature of 150°C. (c) Actuation curvature as a function of the scratch load and the scratch post velocity. The inset shows actuation curvatures versus post velocities at a fixed load of 2.4 g. The shaded areas indicate the control regions we selected to use in surface reconstruction designs.

thickness to 0.2 mm. We have tested other layer thicknesses with our setup. However, other film thicknesses resulted in a much narrower actuation range than the 0.2 mm films that spanned bending radii from 1.8 mm to 14.4 mm. For example, with a layer thickness of 0.1 mm, all the bending radii under different shear velocities and pressures were below 3 mm, which did not offer enough range for actuation into complex shapes. Therefore, 0.2 mm thickness was selected empirically in our setup.

During the alignment process, the mesogens at the top surface reflowed under the shear force from the scratch post. Due to the high viscosity of LCE, there was a small gradient in alignment between the top and bottom of each layer. In constructing the four-layer structure, we specified control inputs to define unique alignment patterns for each layer. We found that we could achieve a desired overall bending curvature without accounting for the variance of the alignment within each layer by calibrating the curvature based on the whole entity of four layers.

In this work, the degree of polymerization (DOP) of the LCE ink was about 7.5. We have tested the free linear contraction strain of LCE with DOP ranging from 7 to 8. The result showed 41%-45% contraction strain, which was a small variance. Therefore, a LCE ink with slightly different DOP composition is acceptable for this work.

2.2. *Defining toolpaths based on curvature directions*

In our patterning approach, the mesogens of the LCE layers were aligned with the moving direction of the scratch post. Hence there was one defined axis of alignment (corresponding to a single axis) for each location on a monodomain LCE surface. Meanwhile, on three-dimensional (3D) structures such as spheres and domes, the surface curvatures at each location may differ depending on directions. Previous studies showed that to form domes with LCE films, azithumal alignment directions is more suitable than radial directions [40–43]. However, while domes were formed during actuation, previous studies have not described a process for controlling the sign of the curvature of the domes (i.e., it was undefined whether the domes would curve upward or downward). Here by aligning two of the four LCE layers, the upward or downward direction of the formed dome can be controlled, which is necessary for generating a complex surface with both concave and convex directions. We aim to demonstrate precise control on actuation directions with our multi-layer designs provide mechanisms to induce up/downward actuation depending on the alignment gradient between layers within the structure.

To determine the optimal curvature directions for patterning the LCE alignment axis, we compare two approaches as illustrated in Fig. 3**(a)**. The schematics include examples at different sampling locations. The bars drawn at each location indicate the magnitudes of local curvature in their respective directions. The curvature is defined as the reciprocal of the bending radius; therefore, a longer bar represents a smaller radius due to a higher bending force upon LCE actuation. The red bar denotes the maximum curvature at a sampling location, while the blue bar represents the curvature perpendicular to the inclined direction (azimuth on the horizontal plane) of the local surface.

We started with a simple goal of patterning a multilayer LCE structure that would transform into a dome upon thermal actuation. We computed two sets of toolpaths for the scratch alignment process, one based on the maximum curvature direction and another one according to the perpendicular counterpart. In the maximum curvature approach, the toolpaths were mostly in radial directions, while in the perpendicular approach, the toolpaths consisted of arc segments [Fig. 3**(b)**]. Note that this divergence of the patterns in the two different approaches only happened in the cases that the dome was more oblate (e.g., vertically

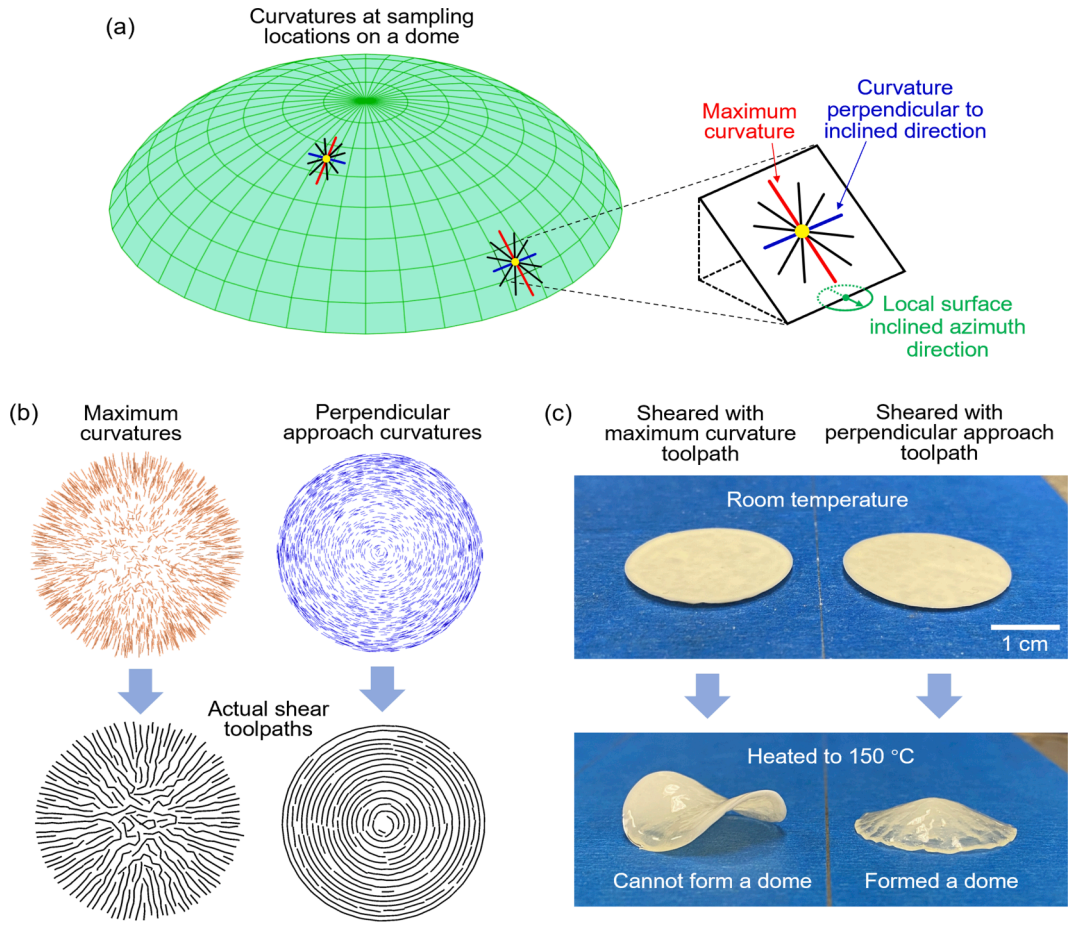

Fig. 3. (a) An illustration of curvatures at different sampling locations on a dome surface (the display grid not drawn to scale). At each sample point (yellow dot), the bar lengths indicate the magnitudes of curvature in specific directions. The red bar indicates the direction of maximum curvature, and the blue bar points in the direction perpendicular to the inclined direction of the local surface. (b) For the dome example, plots of the local maximum curvatures (red) and curvatures perpendicular to surface inclined directions (blue). The black lines indicate the calculated toolpaths for the scratch post for each case. (c) Photographs of LCE samples sheared with toolpaths based on the local maximum (left) or the perpendicular approach (right).

compressed) than a perfect spherical dome. For prolate domes, both approaches lead to circular toolpaths. Samples were patterned with the two toolpath designs, and upon thermal actuation at 150 $^{\circ}C$ in Fig. 3**(c)**, only the sample patterned with the perpendicular approach was able to form a dome, while the other sample based on the maximum curvature direction formed an unexpected saddle shape. This result pointed out that, to form a dome, there should be material contraction along circular contours in addition to curvature formation, and the perpendicular approach for toolpath computation offered this contraction control better than the maximum curvature method.

To demonstrate the ability of our alignment platform to pattern complex freeform surfaces, we targeted the fabrication of LCE stacks that would morph into the shape of a human face, which is fundamentally a combination of multiple domes. For example, the face contour is a large dome, and facial features such as the lips are two stretched domes, the nose is a triangular dome, and the eye sockets are two concave domes. As such, a toolpath design based on the perpendicular approach is promising for this face model demonstration. The goal of reproducing a face has been done before [31] is used as a benchmark for our processing, as our fabrication and control algorithm are distinct from prior works. On account of the complexities of a face model, we developed the following algorithm to generate patterning toolpaths that optimize the fidelity of actuated samples to the intended design.

2.3. Tool path generation

To generate freeform toolpaths for our LCE alignment platform, the computation algorithm involved three main steps as shown in Fig. 4**(a)**. The first step was to calculate the local curvature direction and magnitude at sampling points on the target shape. The second step was to map the positions of the sampling points from the 3D shape to a flat surface using a method that compensates for area distortions. In the last step, the calculations from the first two steps were brought together to determine the toolpath for the scratch post, translating the local curvatures into scratch trajectory, velocity, and load to be implemented on the alignment platform.

Step 1: Calculating local curvature direction and magnitude

For an arbitrary 3D surface to be reconstructed from an actuated LCE stack, for example the face model in our demonstration, we started with the target shape and created a point cloud to represent that 3D surface. The target surface was filled with points such that no more than 0.1 mm was between any two adjacent points, for our design intended to be in the range of a few square centimeters in size. The 0.1 mm point distance was determined by the resolution of our process considering the size of the scratch post, and it is independent from the scale of the model.

We deleted the edges of the 3D model and only used the point cloud for calculations, as shown in Fig. 4**(b)**. Starting from a sampling point P_1, on the selected curvature direction, we estimated the corresponding

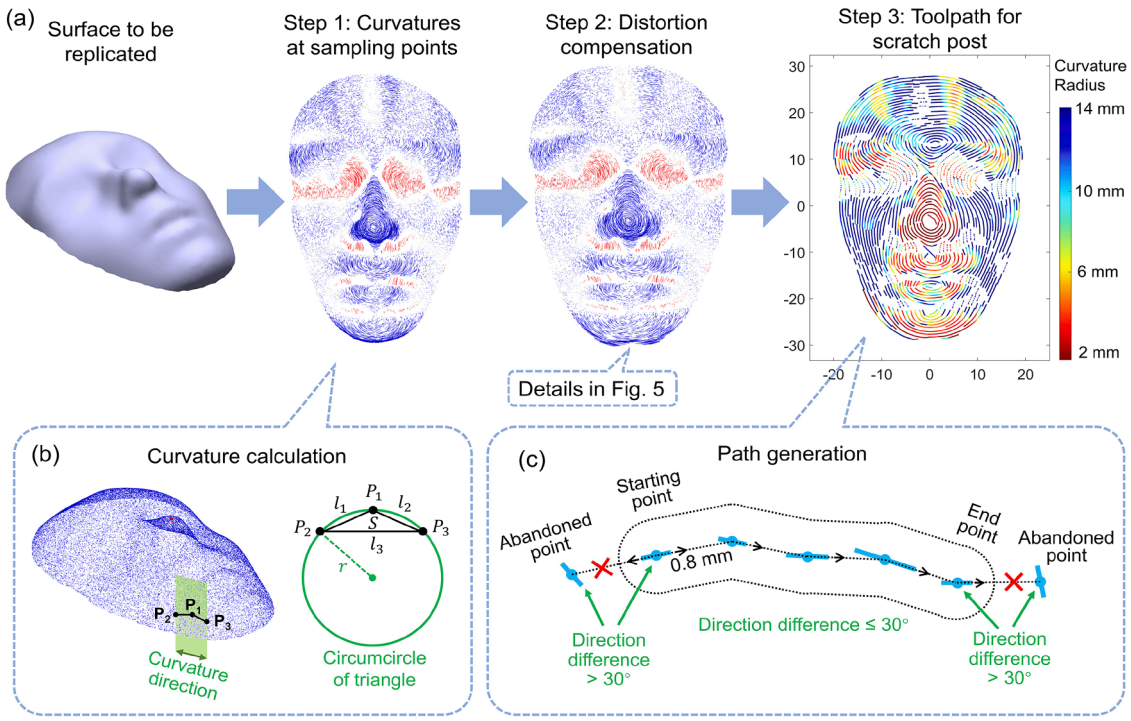

Fig. 4. (a) Process to generate toolpath for patterning the desired 3D surface. In Step 1 and 2, the blue and red colors indicate convex and concave curvatures, respectively. The magnitude of curvature is indicated by the length of each bar. In the toolpath diagram in Step 3, the solid and dashed lines represent convex and concave regions, respectively. (b) Diagram used in calculating the curvature radius at location P_1. (c) A schematic showing the clustering criterion from a group of local points to determine the start and the end of a toolpath pass.

curvature magnitude using two neighboring points, labeled as P_2 and P_3, about 2 mm away from P_1. As shown in Fig. 4(b), the radius of curvature at point P_1 was determined from the circumcircle of the triangle formed by the three points. The actual distances between the three points were calculated from their coordinates and labeled l_1, l_2 and l_3. The radius of curvature was calculated by the following formulas in Equations 1 to 3:

$$\text{Semi}-\text{perimeter of } \triangle P_1P_2P_3: \ l = \frac{l_1 + l_2 + l_3}{2} \tag{1}$$

$$\text{Area of } \triangle P_1P_2P_3: \ S = \sqrt{l(l-l_1)(l-l_2)(l-l_3)} \tag{2}$$

$$\text{Radius of circumcircle}: \ r = \frac{l_1 \times l_2 \times l_3}{4S} \tag{3}$$

In this method, the distance to the two neighboring points (l_1 and l_2) is approximately 2 mm, which was determined by the range of curvatures on the human face 3D model. Other values from 1 mm to 4 mm were also tested, and empirically we found a point spacing of 2 mm to best reproduce the range of curvatures appearing in our target structure. To find the maximum curvature direction, this calculation is repeated for 180 bidirectional orientations around P_1 in 1° intervals, while in the perpendicular approach, the process is executed only once in the pre-selected direction. In both approaches of curvature calculation, if one of the neighboring points P2 or P3 fell at a position outside of the boundary of the curved surface, all the curvatures at point P1 would not be calculated, and P1 would be deleted from the list of candidate points for toolpath generation. The reason is that the boundary of the surface is not considered as a target surface to be achieved in our experiments. Calculation of curvatures across the boundary could cause unstable results, so these points were abandoned. For our toolpath algorithm, we used the curvature direction based on the perpendicular approach, stepping bi-laterally from each sample point. In Fig. 4(a) Step 1, the bars were vectors pointing in the curvature directions calculated form the perpendicular approach, and the bar length represented the magnitude of curvature (1/r) at each sampling point. The blue bars marked the convex surfaces, and the red bars marked the concave regions.

Step 2. Mapping a 3D surface onto a 2D plane and compensating for distortions

In projecting the desired 3D model onto a 2D plane, the relative positions of patterning segments should be shifted as illustrated in Fig. 5 **(a)**. In 3D, the segmentation grid of x-y axes were set in equal spacing. Yet when we flattened the model contours, the segmentation lengths along the x-y axes would no longer be equal but rather depend on slope integrals along the z-axis. For example, a segment with a sharp z-slope would be projected to a long segment (i), and a shallow z-slope to a corresponding short segment at (ii) in Fig. 5(a). The traditional method to correct such changes is through finite element analysis (FEA). Instead of using computationally intensive FEA, below we present a simple and accessible recursive algorithm to correct the area distortions which can be processed by general mathematical programming tools such as MATLAB.

Our process of segment mapping and distortion compensation is shown in Figs. 5(b-f). In the first step, a point cloud representing the target 3D model was set to a x-y grid. Within the boundaries of each grid, all the points were fit to a plane using least square regression. The intersection of the fit plane with the grid axes was a parallelogram. These parallelogram blocks are shown in Fig. 5(b). In the second step, the incline angle of each parallelogram block was computed, and the blocks were rotated to remove the incline with respect to the x-y plane. The side view and the top view after rotation are shown in Figs. 5(c) and 4(d), respectively. Because the sizes of the parallelogram blocks were the same as or larger than the original grid blocks, there were overlaps between the blocks as seen in Fig. 5(d). In the third step, the blocks were translated to eliminate the overlaps which extended the area coverage. For a corner block, the translation involved aligning the shared vertices between this block and the neighboring center block. Meanwhile for an edge block, the translation was implemented to align the mid-point of

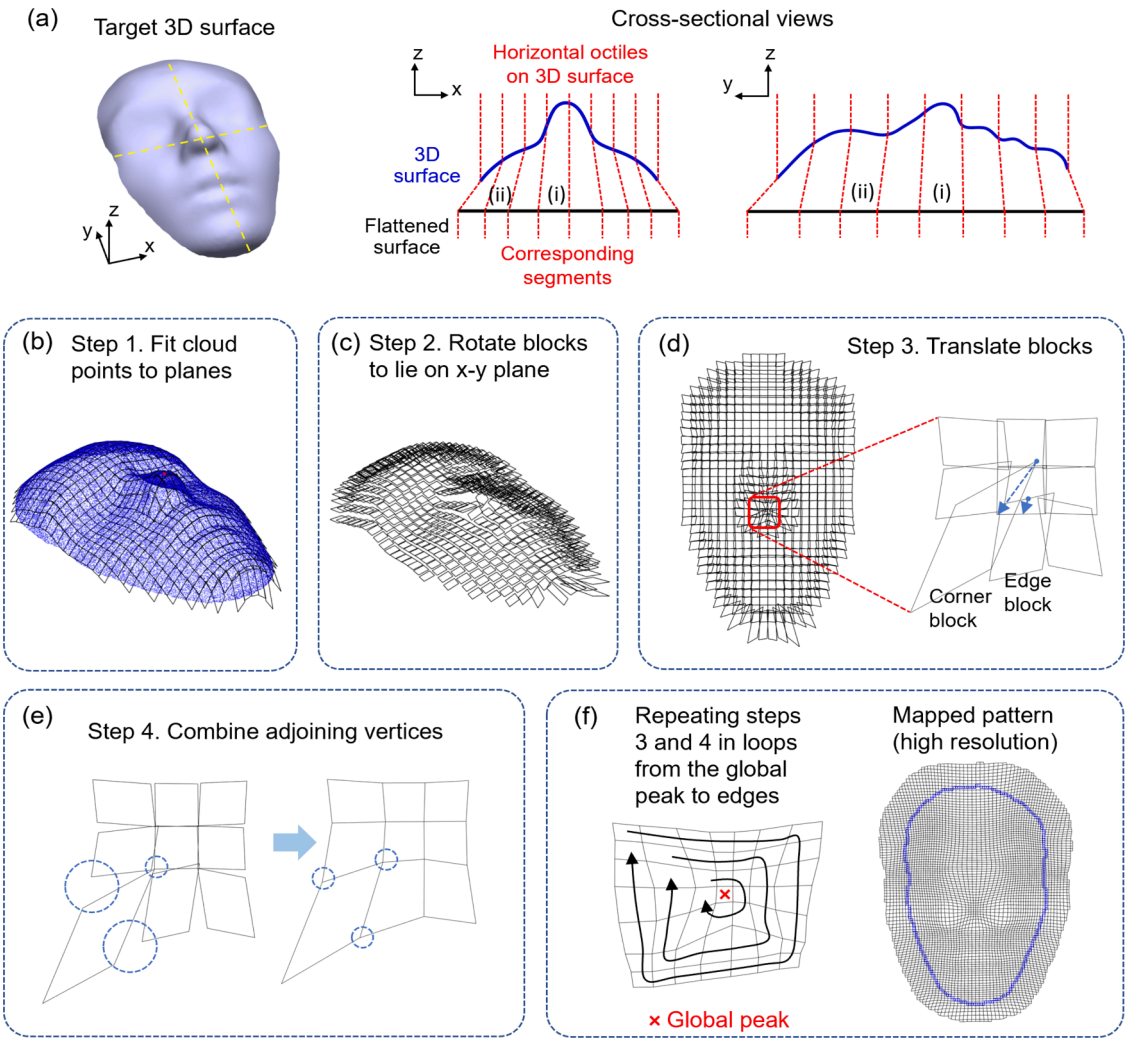

Fig. 5. Distortion compensation process that maps a 3D surface to a flattened plane. In part (a), The cross-sectional views correlate the 3D grid to expanded plane segments at the location denoted by the two yellow dashed lines. Parts (b)—(f) show the calculation steps. In part (f), the outline of the original mesh of the 3D face surface is shown in blue, and the final mesh projected onto a 2D plane is shown in black.

the edge shared with its neighboring block.

After translation of all the blocks surrounding the central one, the result is shown as the left diagram in Fig. 5(e). In the fourth step, to fill the gaps between the blocks, the vertices in blocks sharing the grid intersection were merged together by calculating the geometric mean positions, as indicated by the blue circles in Fig. 5(e). Lastly, steps 3 and 4 were repeated recursively from the block at the global peak to the edges of the whole mesh in loops. The central block at the global peak was found by locating the block highest on the z axis. In each recursive loop, the blocks were first translated based on the inner loop, followed by stitching all the shared vertices. A representative example of the final result after compensating for area distortions is shown in the right diagram of Fig. 5(f), which shows the extended areas in the x-y plane compared to the outline of the initial 3D mesh (blue line). Our process here accounted for the additional LCE material needed to raise the surface and create contours in the z-axis. Finally, the positions of points in the 3D cloud were mapped to the corresponding coordinates projected on the x-y plane, and the local curvature is displayed with distortion compensation in the Step 2 diagram of Fig. 4(a).

Step 3. Translating curvature information into scratch post toolpaths

The algorithm to translate the local curvatures into toolpath trajectories is illustrated in Fig. 4**(c)**. To generate a path, the starting location was a randomly selected point in the point cloud. Next, using the local curvature vectors from Step 2 of Fig. 4(a), the algorithm traversed the plane taking positive and negative steps in the vector direction of the starting point in step sizes of 0.8 mm (the step size was chosen to match the diameter of the scratch post). The algorithm then selected the two cloud points located closest to the endpoints in both directions. The curvature directions of these newly selected points were then retrieved and compared with that of the initial point. If the curvature directions differed by $\leq 30°$, the new point location would be added into the path. Otherwise, the new point location would be dismissed, and the toolpath trajectory would terminate at this location. In Fig. 4(c), the point to the left of the first point was not included, while the point to the right was selected as the second point for this path. The selection of trajectory points was repeated recursively according to this method until the toolpath was terminated at both ends. That is, the toolpath was completed when the differences in curvature direction between the trajectory endpoints and the next candidate points were greater than 30°. Each toolpath would have a line width of 0.8 mm which was the scratch post diameter, as marked by the dashed contour in Fig. 4(c). To prevent other trajectories from overlapping and overwriting the same areas, the algorithm would delete all the cloud points within the line-width contour upon the completion of a trajectory, so that new paths would be generated only from points outside of existing paths.

In generating toolpath trajectories, the algorithm first accounted for

the curvature direction at each sampling point as discussed above. Subsequently, the algorithm incorporated the target curvature magnitudes by controlling the velocity and load of the scratch post, according to the calibration in Fig. 2(c). The resulting toolpath map for our face model is shown in Fig. 4(c); for each trajectory, the spatial changes in the curvature magnitude are denoted by the color scale. In addition, the solid lines indicate paths to form convex surfaces, while the dashed lines show concave regions. To control the LCE actuation to either a convex or concave shape, the algorithm would align the bottom two layers of the 4-layer LCE structures to achieve convex curvatures, or conversely scratch the top two layers for concave surfaces, while leaving the other remaining layers in an unaligned polydomain state.

A more sophisticated material model (e.g., using inverse finite element analysis) could more accurately predict the deformation of the sheet of LCE based on a set of prescribed actuation strains, but this computational refinement will be a future work. The main contribution of this work is an alternate method for aligning the actuation patterns of LCE in a programmable way. Our goal here was to devise a computationally efficient algorithm for patterning a sheet of LCE using our alignment method to achieve a desired deformation with explicit curvature control.

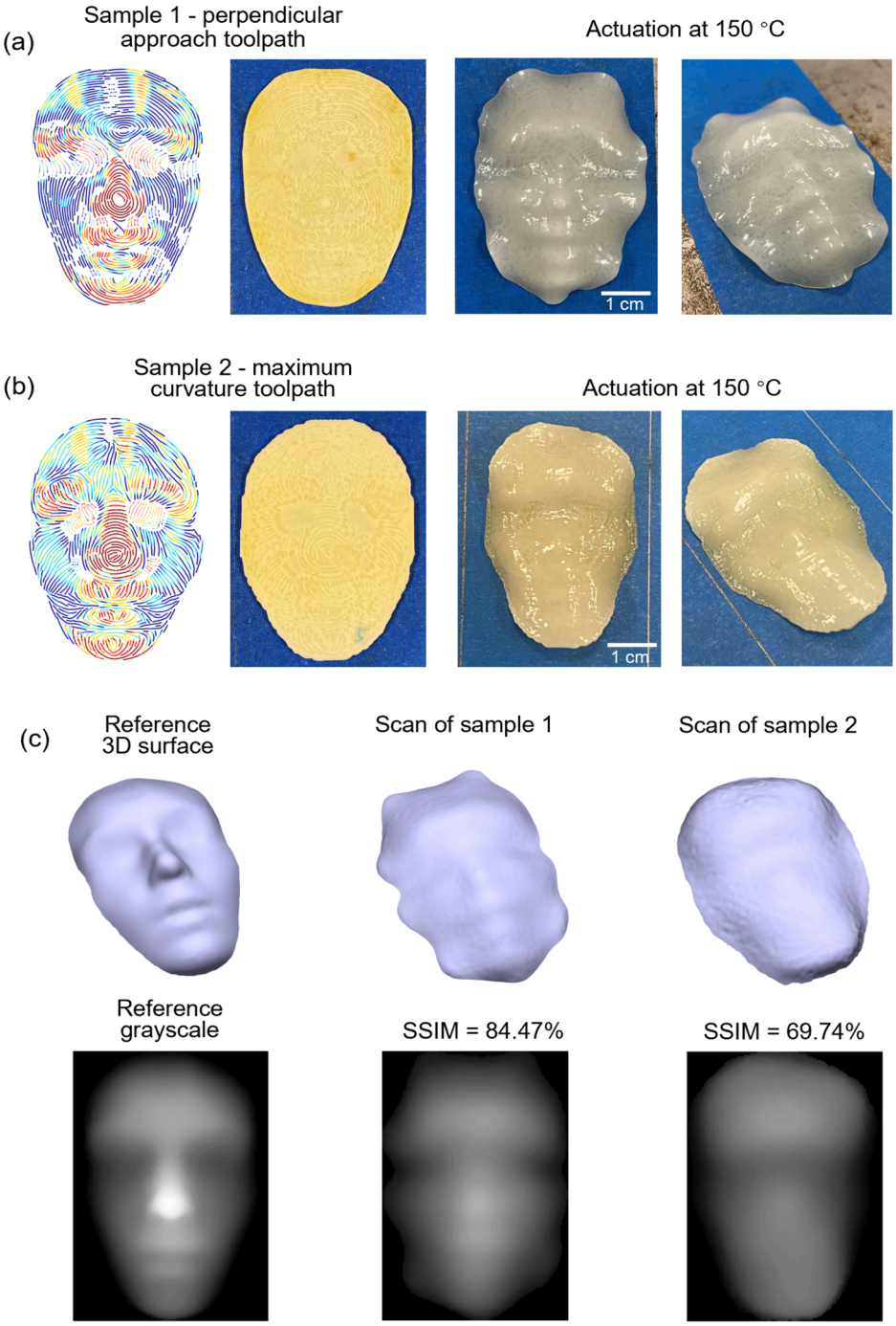

Fig. 6. Toolpath diagrams and photographs of LCE samples patterned according to (a) the perpendicular approach and (b) the local maximum curvature approach. The flat films at room temperature morphed into 3D face structures upon actuation by heating at 150°C. (c) Comparison of the reference 3D surface and the two actuated samples. The first row shows 3D scan results, and the second are grayscale images with their corresponding structural similarity indices.

2.4. Actuation results

We processed LCE samples with the toolpath algorithm in Fig. 4, and photographs of the workpieces at room temperature and at 150 °C are shown in Fig. 6. Upon heat actuation, the LCE samples transformed from a flat film to a 3D surface reproducing the human face model. A video of the actuation process is attached in the supplementary materials as Movie SM2. We compared our two strategies to generate toolpaths, by examining the designs and actuated structures results based on the perpendicular approach and the local maximum curvature approach seen in Fig. 6(a) (sample 1) and 6(b) (sample 2), respectively. Qualitatively, the actuated sample in Fig. 6(a) showed more distinctive features than the one in Fig. 6(b). Also, the latter sample mainly bent along the x-direction while the bending along the y-direction was limited, which was similar to the saddle outcome in Fig. 3(c).

To quantify the degree in similarity of the actuated samples to the target model, the topography of actuated samples were captured via a 3D scanner as shown in the upper row of Fig. 6(c). Then the topography measurements were transferred to grayscale images (104 × 168 pixels) based on the z-axis value at each pixel, shown in the lower row of Fig. 6 (c). The similarities between the images were calculated using the *structural similarity index measure* (SSIM) in Equation 4, used to assess the fidelity of image and video processing [44]. On the reference target and sample images, a pair of 9 × 9 windows were generated at corresponding positions, marked as r and s, respectively. The SSIM value between the two windowed images was calculated by

$$SSIM(r,s) = \frac{(2\mu_r\mu_s)(2\sigma_{rs})}{(\mu_r^2+\mu_s^2)(\sigma_r^2+\sigma_s^2)} \tag{4}$$

where μ_r and μ_s were the means of the two windows, σ_r and σ_s were the variances of the windows, σ_{rs} was the covariance. The windows were shifted through the whole images and the overall SSIM value was determined by the mean value from all the window pairs. In this calculation, we only counted the common areas—if in one window there were non-zero values, yet the corresponding window had all zeros, the SSIM from this pair of windows was not counted in the mean. Finally, the SSIM was 84.5% for sample 1 and only 69.7% for sample 2, confirming that the perpendicular approach improved fidelity for face model reconstruction.

3. Discussion

Our LCE mesogen alignment method and the toolpath algorithm offer freeform reconfigurability to program morphing layers in millimeter resolution. This approach enables the alignment of LCE in patterns with arbitrary direction and magnitude, including areas with no alignment. It is difficult or impossible to achieve these features with prior direct-ink writing approaches while fulfilling close-pack infill in the layer. By programming the scratch post load and velocity, we realized a gradient of actuation strains; this ability to achieve graded mesogen alignment enabled a continuum of bending and linear deformations, providing more control than prior work where the LCE alignment was binary (i.e., it was either maximally aligned or not). In addition, our method allowed facile layer-by-layer patterning to implement precise out-of-plane bending actuation. Previously, linear contraction was the main actuation mode in LCE structures. While contraction around a perimeter had been able to squeeze a LCE film into 3D shapes, such structures was not directly programmed in curvature and actuated arbitrarily between convex or concave forms. In our approach, we have demonstrated how to control both the linear contraction and the bending curvature of a morphed structure. The LCE structure was designed in multiple layers with different extents of mesogen alignment, for the workpiece to actuate by bending with well-defined curvatures. One clear evidence was that the lips on our face model, which were reproduced in the actuation state in Fig. 6(a), which were not obvious in earlier morphing demonstrations [3,31], showcasing that our method met the difficult challenge of patterning convex and concave regions in close proximity.

In our toolpath algorithms, we used the curvature perpendicular to the local incline for trajectory calculations. As tested, this perpendicular approach was more suited than the maximum curvature approach in forming dome-like surfaces in human faces. While the target surface was complex, capturing the curvatures with the perpendicular approach was sufficient to reconstruct the surface with fast prototyping processes, which greatly reduced the calculation iterations spent on toolpath generation. However, as shown in Fig. 6(c), our best reconstruction SSIM was 84.5%, which still shows room for improving the fidelity compared to the intended shape.

One reason for this divergence was that the actuation radius only covered the range from 1.8 mm to 14.4 mm, while among all the curvatures calculated on the 3D face model, 3% of the cloud points were lower and 41% were higher than this range. The 41% of points with a radius of curvature larger than 14.4 mm meant that the points were on a nearly flat plane. We rounded the outliers to the boundary limits, which resulted in lower shape fidelity. A potential solution is to modify the load and velocity of the scratch post to achieve a wider range of radii. Alternately, in the fabrication process, all four layers of LCE can be aligned in different patterns to enhance bending or linear actuation. For example, if the first three layers were aligned and only the fourth layer remained polydomain, the whole film may bend beyond the current limits. Likewise, if all four layers were scratched with the same parameters, the aligned region would undergo linear in-plane contraction. Another contribution to the fidelity loss was that some minor information of surface bending and area mapping was lost when we used the perpendicular approach to calculate toolpath trajectories. A possible improvement would be to use finite element analysis to calculate all the surface bending and area mapping with a denser mesh than the one implemented here. This approach would be much more computationally expensive, but could improve the SSIM.

In our surface reproduction experiment, we scaled the original face model to the size of about 4 cm by 6 cm. The total travel distance of the corresponding scratching toolpath for the convex bending layer (solid paths in Step 3 of Fig. 4(a)) was about 2700 mm, which took about one hour to finish. By empirical testing, the alignment in uncured LCE could maintain for 2-3 hours before turning to polydomain state. Therefore, we scaled the target model to limit the scratching process of any single layer within one hour, so the whole layer can be cured by UV before the aligned pattern disappeared. If a pattern in a larger scale is required, one possible approach is to grid and separate the pattern into multiple small segments.

In summary, we demonstrated a freeform LCE alignment system which transferred high-fidelity patterns with large strain gradients. The toolpath algorithm reconstructed 3D shapes by bending curvature control in multi-layered structures, expanding beyond conventional linear contraction control and the limits of single films. With the low-cost setup and easy implementation, this versatile fabrication approach has the potential to enable high-precision, reconfigurable LCE structures in future applications.

4. Materials and Methods

4.1. Preparation of LCE ink

The LCE ink was synthesized from monomer 1,4-bis-[4-(3-acryloyloxypropyloxy) benzoyloxy]-2-methylbenzene (RM257, 98.8%, Wilshire technologies) and 2,2′-(ethylenedioxy) diethanethiol (EDDET, 90∼95%, Sigma-Aldrich). The chemical structures and differential scanning calorimetry of the LCE ink are included in the Supplemental Figure S1. The degree of polymerization of the ink was targeted to be 7∼8. First, 0.04 mole of RM257 and 0.035 mole of EDDET were dissolved in 100 mL dichloromethane. Then 0.54 mL dipropylamine was

added into the solution as the polymerization catalyst. The solution was stirred for 24 hours at room temperature. Subsequently, 0.11 g 2-hydroxy-4′-(2-hydroxyethoxy)-2-methylpropiophenone was added to the solution as a photo initiator. In a round bottom flask, the solution was stirred and heated to 70°C on a heating mantle (Mtops DMS632) to evaporate the solvent. In 30 minutes, most of the solvent was removed, and then the flask was connected to vacuum and heated to 90°C for one day to remove residual solvent and catalyst. During heating, the flask was covered by aluminum foils to avoid crosslinking induced by florescent lights in the room. After solvent evaporation, the LCE ink was loaded into a 10 mL dispensing syringe. A hot air gun set to 200°C was used to heat the flask to reduce the ink viscosity in order for it to flow out. Then the dispensing syringe was held vertically and heated in an oven to 80°C for 24 hours, for the ink to settle and de-gas.

4.2. Fabrication process

Each sample consisted of four LCE layers printed on glass substrates, with each layer extruded to be 0.2 mm in thickness. To remove alignment due to the shear force from the extrusion nozzle, each layer was heated for 1 min with a hot air gun at 120°C to reset LCE mesogens to isotropic polydomains. Then the film was patterned by the scratch post to align mesogens according to the selected toolpath. After the alignment process, the film was cured under 10 Watts 365 nm UV light for 3 minutes to crosslink the LCE. The deposition and alignment steps were repeated for each layer. After completing all the four layers, on the rectangular film, we cut the outer unaligned region along the perimeter of the patterned region by scissors. Further reproducing and scanning were based on the film with the patterned region only.

4.3. 3D scanning of actuated samples

The samples were heated on a hot plat at 150°C to actuate shape morphing. The TrueDepth camera on an iPhone 11 Pro was used to scan the actuated workpiece as recorded by the “Capture” App. The scan result was a point cloud in obj format. The point cloud was then transferred to a continuous 3D mesh by the “MeshLab” program and saved as an stl file.

Data Availability

The raw data required to reproduce these findings are available upon request. Please send any request to the corresponding author.

CRediT authorship contribution statement

Yichen Zhai: Conceptualization, Methodology, Software, Writing – original draft. **Michael T. Tolley:** Formal analysis, Writing – review & editing. **Tse Nga Ng:** Supervision, Formal analysis, Writing – review & editing.

Declaration of Competing interest

The authors declare that they have no known competing financial interests or personal relationships that could have appeared to influence the work reported in this paper.

Acknowledgment

The authors thank Zijun Wang in Prof. Shengqiang Cai’s lab for conducting the DSC measurements. This work was partially supported by a visiting scholar grant from Samsung Electronics.

Supplementary materials

Supplementary material associated with this article can be found, in the online version, at doi:10.1016/j.apmt.2022.101501.

References

[1] I. Jung, J. Xiao, V. Malyarchuk, C. Lu, M. Li, Z. Liu, J. Yoon, Y. Huang, J.A. Rogers, Dynamically tunable hemispherical electronic eye camera system with adjustable zoom capability, Proceedings of the National Academy of Sciences 108 (2011) 1788–1793.
[2] Y. Qiu, E. Zhang, R. Plamthottam, Q. Pei, Dielectric Elastomer Artificial Muscle: Materials Innovations and Device Explorations, Accounts of Chemical Research 52 (2019) 316–325.
[3] J.W. Boley, W.M. Van Rees, C. Lissandrello, M.N. Horenstein, R.L. Truby, A. Kotikian, J.A. Lewis, L. Mahadevan, Shape-shifting structured lattices via multimaterial 4D printing, Proceedings of the National Academy of Sciences of the United States of America 116 (2019) 20856–20862.
[4] R. Su, S.H. Park, Z. Li, M.C. McAlpine, Robotic Systems and Autonomous Platforms, Elsevier Ltd., 2019, pp. 309–334.
[5] T.J. Wallin, J. Pikul, R.F. Shepherd, 3D printing of soft robotic systems, Nature Reviews Materials 3 (2018) 84–100.
[6] J.H. Pikul, S. Li, H. Bai, R.T. Hanlon, I. Cohen, R.F. Shepherd, Stretchable surfaces with programmable 3D texture morphing for synthetic camouflaging skins, Science 358 (2017) 210–214.
[7] D. Rus, M.T. Tolley, Design, fabrication and control of soft robots, Nature 521 (2015) 467.
[8] Y. Zhai, Z. Wang, K.S. Kwon, S. Cai, D. Lipomi, T.N. Ng, Printing Multi-Material Organic Haptic Actuators, Advanced Materials 33 (2020), 2002541.
[9] Y. Liu, J. Li, S. Song, J. Kang, Y. Tsao, S. Chen, V. Mottni, K. McConnell, W. Xu, Y.-Q. Zheng, J.B.-H. Tok, P.M. George, Z. Bao, Morphing electronics enable neuromodulation in growing tissue, Nature Biotechnology 38 (2020) 1031–1036.
[10] D.-H. Kim, N. Lu, R. Ma, Y.-S. Kim, R.-H. Kim, S. Wang, J. Wu, S.M. Won, H. Tao, A. Islam, K.J. Yu, T. Kim, R. Chowdhury, M. Ying, L. Xu, M. Li, H.-J. Chung, H. Keum, M. Mccormick, P. Liu, Y. Zhang, F.G. Omenetto, Y. Huang, T. Coleman, J. A. Rogers, Epidermal Electronics, Science 333 (2011) 838–844.
[11] E. Yarali, M. Baniasadi, A. Zolfagharian, M. Chavoshi, F. Arefi, M. Hossain, A. Bastola, M. Ansari, A. Foyouzat, A. Dabbagh, M. Ebrahimi, M.J. Mirzaali, M. Bodaghi, Magneto-/electro-responsive polymers toward manufacturing, characterization, and biomedical/ soft robotic applications, Applied Materials Today 26 (2022), 101306.
[12] K. Fuchi, T.H. Ware, P.R. Buskohl, G.W. Reich, R.A. Vaia, T.J. White, J.J. Joo, Topology optimization for the design of folding liquid crystal elastomer actuators, Soft Matter 11 (2015) 7288–7295.
[13] Y. Guo, H. Shahsavan, M. Sitti, 3D Microstructures of Liquid Crystal Networks with Programmed Voxelated Director Fields, Advanced Materials 32 (2020) 1–10.
[14] T.H. Ware, M.E. McConney, J.J. Wie, V.P. Tondiglia, T.J. White, Voxelated liquid crystal elastomers, Science 347 (2015) 982–984.
[15] Y. Xia, G. Cedillo-Servin, R.D. Kamien, S. Yang, Guided Folding of Nematic Liquid Crystal Elastomer Sheets into 3D via Patterned 1D Microchannels, Advanced Materials 28 (2016) 9637–9643.
[16] O.D. Lavrentovich, Prepatterned liquid crystal elastomers as a step toward artificial morphogenesis, Proceedings of the National Academy of Sciences of the United States of America 115 (2018) 7171–7173.
[17] E.C. Davidson, A. Kotikian, S. Li, J. Aizenberg, J.A. Lewis, 3D Printable and Reconfigurable Liquid Crystal Elastomers with Light-Induced Shape Memory via Dynamic Bond Exchange, Advanced Materials 1905682 (2019).
[18] Y. Zhang, Z. Wang, Y. Yang, Q. Chen, X. Qian, Y. Wu, H. Liang, Y. Xu, Y. Wei, Y. Ji, Seamless multimaterial 3D liquid-crystalline elastomer actuators for next-generation entirely soft robots, Science Advances 6 (2020) eaay8606.
[19] Q. He, Z. Wang, Y. Wang, A. Minori, M.T. Tolley, S. Cai, Electrically controlled liquid crystal elastomer-based soft tubular actuator with multimodal actuation, Science Advances 5 (2019) eaax5746.
[20] Y. Zhai, N.T. Ng, Self-Sustained Robots Based on Functionally Graded Elastomeric Actuators Capable of Carrying a Payload 22 Times of Body-Weight, Advanced Intelligent Systems (2021), 2100085.
[21] Z.Z. Nie, B. Zuo, M. Wang, S. Huang, X.M. Chen, Z.Y. Liu, H. Yang, Light-driven continuous rotating Möbius strip actuators, Nature Communications 12 (2021), https://doi.org/10.1038/s41467-021-22644-9.
[22] Y. Huang, H.K. Bisoyi, S. Huang, M. Wang, X.M. Chen, Z. Liu, H. Yang, Q. Li, Bioinspired Synergistic Photochromic Luminescence and Programmable Liquid Crystal Actuators, Angewandte Chemie - International Edition 60 (2021) 11247–11251.
[23] V. Agostiniani, A. DeSimone, Rigorous derivation of active plate models for thin sheets of nematic elastomers, Mathematics and Mechanics of Solids 25 (2020) 1804–1830.
[24] R. Brighenti, C.G. McMahan, M.P. Cosma, A. Kotikian, J.A. Lewis, C. Daraio, A micromechanical-based model of stimulus responsive liquid crystal elastomers, International Journal of Solids and Structures 219–220 (2021) 92–105.
[25] F. Cirak, Q. Long, K. Bhattacharya, M. Warner, Computational analysis of liquid crystalline elastomer membranes: Changing Gaussian curvature without stretch energy, International Journal of Solids and Structures 51 (2014) 144–153.
[26] X. Liang, D. Li, A Programmable Liquid Crystal Elastomer Metamaterials With Soft Elasticity, Frontiers in Robotics and AI 9 (2022) 1–12.
[27] M.J. Ford, C.P. Ambulo, T.A. Kent, E.J. Markvicka, C. Pan, J. Malen, T.H. Ware, C. Majidi, A multifunctional shape-morphing elastomer with liquid metal inclusions, Proceedings of the National Academy of Sciences of the United States of America 116 (2019) 21438–21444.

[28] M. Barnes, R. Verduzco, Direct shape programming of liquid crystal elastomers, Soft Matter 15 (2019) 870–879.
[29] Q. Li, R. Sun, A.Le Duigou, J. Guo, J. Rossiter, L. Liu, J. Leng, F. Scarpa, Programmable and reconfigurable hygro-thermo morphing materials with multifunctional shape transformation, Applied Materials Today 27 (2022), 101414.
[30] K. Kwon, T.N. Ng, Improving Electroactive Polymer Actuator by Tuning Ionic Liquid Concentration, Organic Electronics 15 (2014) 294–298.
[31] H. Aharoni, Y. Xia, X. Zhang, R.D. Kamien, S. Yang, Universal inverse design of surfaces with thin nematic elastomer sheets, Proceedings of the National Academy of Sciences of the United States of America 115 (2018) 7206–7211.
[32] W. Wang, Mechanical Assembly of Thermo-Responsive Polymer-Based Untethered Shape-Morphing Structures, Macromolecular Materials and Engineering 305 (2020), 1900568.
[33] M.T. Tolley, S.M. Felton, S. Miyashita, D. Aukes, D. Rus, R.J. Wood, Self-folding origami: Shape memory composites activated by uniform heating, Smart Materials and Structures 23 (2014), 094006.
[34] A. Minori, S. Jadhav, Q. He, S. Cai, M.T. Tolley, Reversible actuation of origami inspired composites using liquid crystal elastomers, in: ASME 2017 Conference on Smart Materials, Adaptive Structures and Intelligent Systems, SMASIS, 2017, https://doi.org/10.1115/SMASIS2017-3986.
[35] A.S. Kuenstler, Y. Chen, P. Bui, H. Kim, A. DeSimone, L. Jin, R.C. Hayward, Blueprinting Photothermal Shape-Morphing of Liquid Crystal Elastomers, Advanced Materials 32 (2020), 2000609.
[36] A.D. Auguste, J.W. Ward, J.O. Hardin, B.A. Kowalski, T.C. Guin, J.D. Berrigan, T. J. White, Enabling and Localizing Omnidirectional Nonlinear Deformation in Liquid Crystalline Elastomers, Advanced Materials 30 (2018), 1802438.
[37] C.M. Yakacki, M. Saed, D.P. Nair, T. Gong, S.M. Reed, C.N. Bowman, Tailorable and programmable liquid-crystalline elastomers using a two-stage thiol-acrylate reaction, RSC Advances 5 (2015) 18997–19001.
[38] A. Kotikian, R.L. Truby, J.W. Boley, T.J. White, J.A. Lewis, 3D Printing of Liquid Crystal Elastomeric Actuators with Spatially Programed Nematic Order, Advanced Materials 30 (2018), 1706164.
[39] Z. Wang, Z. Wang, Y. Zheng, Q. He, Y. Wang, S. Cai, Three-dimensional printing of functionally graded liquid crystal elastomer, Science Advances 6 (2020) eabc0034.
[40] G.F. Hu, A.R. Damanpack, M. Bodaghi, W.H. Liao, Increasing dimension of structures by 4D printing shape memory polymers via fused deposition modeling, Smart Materials and Structures 26 (2017), https://doi.org/10.1088/1361-665X/aa95ec.
[41] L.T. De Haan, C. Sánchez-Somolinos, C.M.W. Bastiaansen, A.P.H.J. Schenning, D. J. Broer, Engineering of complex order and the macroscopic deformation of liquid crystal polymer networks, Angewandte Chemie - International Edition 51 (2012) 12469–12472.
[42] C.D. Modes, M. Warner, Blueprinting nematic glass: Systematically constructing and combining active points of curvature for emergent morphology, Physical Review E 84 (2011), 021711.
[43] N.P. Godman, B.A. Kowalski, A.D. Auguste, H. Koerner, T.J. White, Synthesis of Elastomeric Liquid Crystalline Polymer Networks via Chain Transfer, ACS Macro Letters 6 (2017) 1290–1295.
[44] Z. Wang, A.C. Bovik, H.R. Sheikh, E.P. Simoncelli, Image quality assessment: From error visibility to structural similarity, IEEE Transactions on Image Processing 13 (2004) 600–612.